A Current Index Approach to Compensate Commutation Phase Error for Sensorless Brushless DC Motors With Nonideal Back EMF

An-Chen Lee, Samuel Wang, and Chia-Juei Fan

***Abstract*—Commutation phase errors during implementation are inevitable in the sensorless drive of the brushless dc (BLDC) motor. This paper analyzed the current waveform during the conducting phase under commutation phase error and nonideal back electromotive force (EMF). The relation between the elapsed time of the commutation phase error with the current waveform, the supplied voltage, and the nonideal back-EMF is derived. Based on this relationship, a reliable optimization method for commutation phase errors compensation is presented. Such method is to minimize the elapsed time of the commutation phase error with robustness properties with respect to parameter variations. In such a way, the peak values of the current at the front and back of the current waveform at each conducting period become more identical, which leads to minimum torque ripple. A digital signal processor-based sensorless BLDC motor controller to implement the proposed method is developed to verify its effectiveness experimentally. Experiment results showed that the proposed sensorless drive is capable of running in different speed and load torque with good performance.**

***Index Terms*—Back electromotive force (EMF), brushless dc (BLDC) motor, commutation phase error, nonideal back electromotive force, pulsating current, sensorless drive.**

I. Introduction

BRUSHLESS dc (BLDC) motors have an advantage over brushed dc in torque performance, noise, operating life, dynamic response, efficiency, and reliability [1]. Position sensors such as Hall-effect sensors are employed to provide rotor position information for commutation, yet misalignment in sensors, running in extreme ambient conditions, or electromagnetic interference introduce error in the position information [1]. Sensorless drive schemes which determine the commutation instant based on characteristics of the BLDC motors such as the zero-crossing points of back electromotive forces (EMFs) were proposed. These techniques can be classified into three categories [1]: direct back EMF detection [2]–[5], indirect back EMF detection [6], [7], and the techniques using model-based estimation [8]–[11]. Each of the back EMF detection methods has their strength in different applications; however, commutation phase errors are still inevitable.

There exist a variety of error sources during implementation, including phase shift from filters [12]–[19], measurement noise from sensors and quantization error from the analog digital converter (ADC) [11], [12], [15], errors from circuit components [7], [13], [20], voltage spikes due to the residual current [18], [19], and limited calculation frequency in the digital signal processor (DSP) or microcontroller. Parameter uncertainty in model-based estimation techniques might also introduce commutation phase error; possible sources come from the variation between the estimated value and the actual value or the changes of the parameters due to environmental factors; in particular, the stator resistance increases with the increase of temperature, and the inductance depends on the load current [8]–[11], [21]. On the other hand, commutation phase error compensation has been investigated in many papers. Shen and Tseng [13] analyzed the rotor position error between different rotor structures and loading conditions; and the authors proposed a compensation circuit to correct the position signal. Yet this paper only concerns the error caused by rotor saliency and low-pass filtering. Bhogineni and Rajagopal [19] analyzed and compensated the commutation error sources including armature winding resistance drop and delay of the low-pass filter, but without an overall error correction method. Jang and Kim [22] presented a method to improve the commutation instant by utilizing the symmetric property of the terminal voltages in the nonconducted phase, yet it requires high ADC sampling frequency. Wu *et al.* [23] proposed a control method using the circulating current as an index for compensation. The circulating current is symmetric when the commutation instant is aligned with the back EMF. However, this method is not suitable for advanced pulse width modulation (PWM) technique application such as PWM_ON_PWM mode, under which circulating current occurrence is avoided [24]. Besides, the magnitude of the circulating current in the nonconducting phase is small during the low-speed operation, where any measurement error will deteriorate the performance. Fang *et al.* [25] used the dc-link current before and after commutation instant to estimate the commutation time error and compensated the initial Hall signal; the method relied on linear relationship between the dc-link current difference and the commutation error in low-inductance motor, and accurate sampling current data. Song and Choy [26] estimated the neutral voltage for commutation error compensation. However, accurate neutral voltage estimation is hard to achieve due to parameter variation and nonideal back EMF. Chen and Liaw [27] proposed an

Manuscript received January 26, 2015; accepted August 5, 2015. Date of publication August 13, 2015; date of current version January 7, 2016. This work was supported by the Ministry of Science and Technology of the Republic of China, under Contract MOST 103-2221-E-009-124-MY2. Recommended for publication by Associate Editor V. Staudt.

The authors are with the Department of Mechanical Engineering, National Chiao Tung University, Hsinchu 300, Taiwan (e-mail: aclee@mail.nctu.edu.tw; samuel6113@hotmail.com; feelmysoul@livemail.tw).

Color versions of one or more of the figures in this paper are available online at http://ieeexplore.ieee.org.

Digital Object Identifier 10.1109/TPEL.2015.2468081

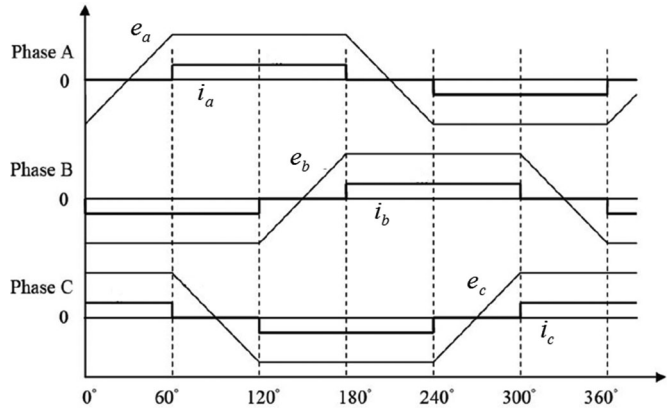

Fig. 1. Relationship between back EMF and current waveform.

intelligent commutation tuning method by minimizing line current, yet the method could be influenced by the inherent phase difference between the terminal voltage and exact back EMF.

The aforementioned commutation phase errors could not be found and compensated at one time completely. Fortunately, the effect of these errors reflects on the commutation instants; the commutation phase error leads to the pulsating current. The nonideal back EMF waveform due to specific reasons such as nonuniformity of the magnetic material and design tradeoff [28], results in the crown-shaped current waveform instead of ideally rectangular. When the effects of the commutation phase error and the nonideal back EMF on current waveforms are considered, a reliable optimization method reflecting the commutation phase error with robustness properties to parameter variations for commutation phase errors compensation is proposed in this paper. Besides, the proposed method can be utilized to derive the equivalent flat-top width of the approximated back EMF.

II. CI Approach

The current waveform under the commutation phase error is demonstrated in the first place, and then, the relationship between the commutation phase error, current waveform, and nonideal back EMF is evaluated. The proposed method is presented in Section II-C. To our surprise, a large number of studies are based on the assumption that the flat-top width of the back EMF waveform is to be ideal 120°; however, the actual waveform of the back EMF might not work as desired. After the current waveform under nonideal back EMF and commutation phase error is comprehensively studied, the proposed current index (CI) approach is presented.

A. Current Waveform Under the Commutation Phase Error

Figs. 1 and 2 show the relationship among the ideal back EMF and current waveform, the equivalent circuit of the BLDC motor, and the three-phase inverter. The surface-mounted permanent magnet rotor structure is considered in this paper, i.e., the stator resistances in the three windings are identical and the mutual inductances are constant [13]. The phase voltage equations are

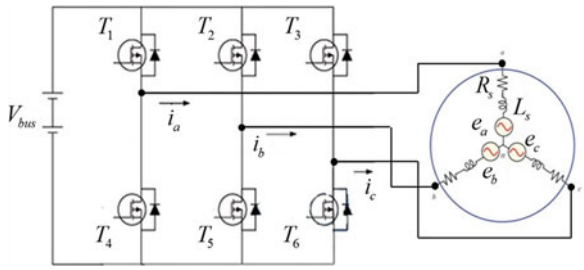

Fig. 2. PWM inverter and the equivalent circuit of the BLDC motor.

shown as

$$\begin{bmatrix} V_{an} \\ V_{bn} \\ V_{cn} \end{bmatrix} = \begin{bmatrix} R_s & 0 & 0 \\ 0 & R_s & 0 \\ 0 & 0 & R_s \end{bmatrix} \begin{bmatrix} i_a \\ i_b \\ i_c \end{bmatrix} + \begin{bmatrix} L_s & 0 & 0 \\ 0 & L_s & 0 \\ 0 & 0 & L_s \end{bmatrix} \frac{d}{dt} \begin{bmatrix} i_a \\ i_b \\ i_c \end{bmatrix} + \begin{bmatrix} e_a \\ e_b \\ e_c \end{bmatrix} \quad (1)$$

$$L_s = L_{ss} - L_m \quad (2)$$

where V_{an}, V_{bn}, and V_{cn} are phase voltages, e_a, e_b, and e_c are back EMFs of each phase, R_s is the phase resistance, L_s is the equivalent inductance in the stator windings, and L_{ss} and L_m are inductance of each phase and mutual inductance between phases, respectively.

Referring to Fig. 1, we consider the case when phase A current is conducting during the commutation interval of 60° to 180°. The following derivation demonstrates the outcome when delay commutation occurs. The other two phases can be obtained by the same token. The influence from the circulating current is assumed to be ignored; during 60°–120° period, when phases A and B are conducting with the phase C floating, the terminal voltage and the current can be expressed as follows:

$$\begin{cases} V_a = V_{\text{bus}} \cdot S = i_a Z + e_a + V_n \\ V_b = i_b Z + e_b + V_n = 0 \\ V_c = e_c + V_n \end{cases} \quad (3)$$

$$i_a = -i_b \quad (4)$$

where Z denotes the impedance of the circuit, V_{bus} is the dc supply voltage, V_n is the neutral voltage, and S represents the switching function of PWM. From (3) and (4), the current during 60° to 120° can be derived as

$$i_a = \frac{V_{\text{bus}} \cdot S - (e_a - e_b)}{2Z}_{(60° \sim 120°).} \quad (5)$$

As shown in Fig. 1, 120° is one of the commutation points, where

$$e_a = -e_b = -e_c. \quad (6)$$

In this case, currents should have a rectangular waveform in the period of 60° to 180°, as shown in Fig. 3(a). However, if the commutation phase error, defined as β in Fig. 3(b) and (c),

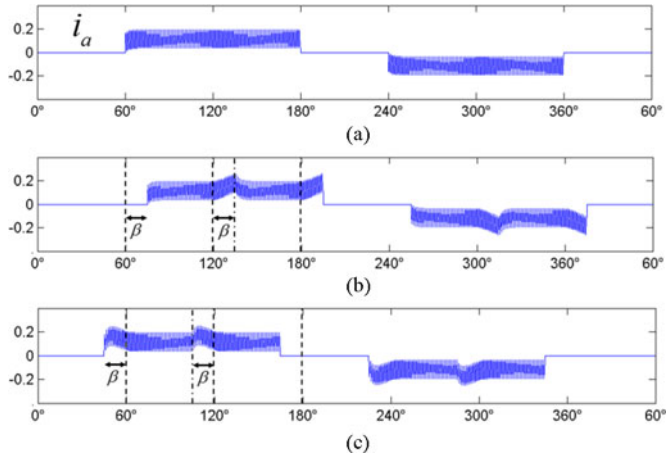

Fig. 3. Current waveforms of phase A under different commutation situations. (a) Ideal commutation. (b) Delay commutation of 15°. (c) Lead commutation of 15°.

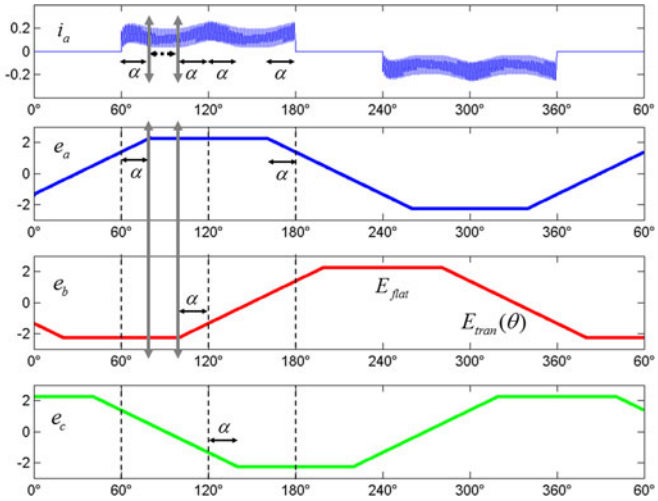

Fig. 4. 80° flat back EMF and corresponding current waveform of phase A.

occurs, the commutation instant will not be at 120° sharp, but at $120 + \beta°$. The relationship between the back EMFs during the delay period is shown as

$$e_a = -e_c > -e_b \qquad \text{for} \quad 120° \sim 120° + \beta. \tag{7}$$

The current waveform of phase A with delay commutation thus becomes

$$i_a = \underset{(60°+\beta\sim 120°)}{\frac{V_{\text{bus}} \cdot S - (e_a - e_b)}{2Z}} < \underset{(120°\sim 120°+\beta).}{\frac{V_{\text{bus}} \cdot S - (e_a - e_b)}{2Z}} \tag{8}$$

Therefore, a pulsating current occurs in phase A, increasing with the current magnitude and delay time. Similarly, during 120°–180° period, when phases A and C are conducting and the phase B is floating, the current can be derived as

$$i_a = \underset{(120°\sim 180°).}{\frac{V_{\text{bus}} \cdot S - (e_a - e_c)}{2Z}} \tag{9}$$

The commutation instant will not be at 180° sharp if phase delay occurs. With the same token in (6) and (7), the back EMFs of phases A and C are no longer identical; the current during this conducting period thus becomes

$$i_a = \underset{(120°+\beta\sim 180°)}{\frac{V_{\text{bus}} \cdot S - (e_a - e_c)}{2Z}} < \underset{(180°\sim 180°+\beta).}{\frac{V_{\text{bus}} \cdot S - (e_a - e_c)}{2Z}} \tag{10}$$

A pulsating current is also produced during this period, increasing with the current magnitude and delay time. On the other hand, as shown in Fig. 3(c), the current waveform with lead commutation can be shown as

$$i_a = \underset{(60°-\beta\sim 60°)}{\frac{V_{\text{bus}} \cdot S - (e_a - e_b)}{2Z}} > \underset{(60°\sim 120°-\beta)}{\frac{V_{\text{bus}} \cdot S - (e_a - e_b)}{2Z}}$$

$$i_a = \underset{(120°-\beta\sim 120°)}{\frac{V_{\text{bus}} \cdot S - (e_a - e_c)}{2Z}} > \underset{(120°\sim 180°-\beta).}{\frac{V_{\text{bus}} \cdot S - (e_a - e_c)}{2Z}} \tag{11}$$

For lead commutation, the pulsating currents occur at $60 - \beta°$–60° period and $120 - \beta°$–120° period. As shown in (8), (10), (11), and Fig. 3(b) and (c), one can discover that the current waveform curls up in the region where the commutation phase error exists, i.e., $\beta \neq 0$.

B. Current Waveform Under Nonideal Back EMF

So far the back EMF waveform is considered to have 120° flat-top width, which means that the air-gap flux distribution is taken as ideal rectangular. Yet, different permanent magnet design of the rotor may produce different air-gap flux distribution. For different rotor magnetic design, parallel magnetization produces a sinusoidal air-gap flux distribution, while radial magnetization produces a near-ideal rectangular distribution. Interlacing a higher energy magnet segment at the pole tips can be employed to reduce the flux leakage and thus achieve a more rectangular air-gap flux distribution [28]. Fig. 4 presents the 80° flat back EMF and corresponding current waveform of phase A. For a nonideal back EMF, where α is defined as the angle deviated from ideal 120° flat back EMF in one side, i.e., the total flat-top width will be $120° - 2\alpha$, as shown in Fig. 4. The back EMF value of the flat-top area is

$$E_{\text{flat}} = K_e \omega. \tag{12}$$

and the transient state, i.e., the straight line around the zero-crossing, is defined as

$$E_{\text{tran}}(\theta) = \pm K_e \omega \mp \frac{6K_e\omega}{\pi + 6\alpha}\theta. \tag{13}$$

where K_e is the back EMF constant, ω is the synchronous speed of the motor, and θ is the angle displacement from the flat-top ending point. During 60°–120° period, the relationship between

the back EMFs can be expressed as

$$(e_a - e_b)_{(60^\circ\sim 60^\circ+\alpha)}, \quad (e_a - e_b)_{(120^\circ-\alpha\sim 120^\circ)} < (e_a - e_b)_{(60^\circ+\alpha\sim 120^\circ-\alpha)}. \tag{14}$$

Note that (14) is used as shorthand that the two terms of the left-hand side of the equation are both smaller than the term of the right-hand side.

As shown in Fig. 4, the current waveform thus becomes

$$i_{a(60^\circ\sim 60^\circ+\alpha)}, \quad i_{a(120^\circ-\alpha\sim 120^\circ)} > i_{a(60^\circ+\alpha\sim 120^\circ-\alpha)}. \tag{15}$$

Similarly, the relationship of the current waveform during 120°–180° period can be expressed as

$$i_{a(120^\circ\sim 120^\circ+\alpha)}, \quad i_{a(180^\circ-\alpha\sim 180^\circ)} > i_{a(120^\circ+\alpha\sim 180^\circ-\alpha)}. \tag{16}$$

As one can discover in (15), (16), and Fig. 4, the current waveform under a narrower back EMF flat-top width curls up at (60°∼60°+α), (120° −α∼120°), (120°∼120°+α), and (180° −α∼180°), period; the waveform during 60° –180° thus appears to be crown shape. Moreover, as one can observe the width of the current waveform valley denoted by dashed black two-way arrow will vary with the overlapped flat-top region of two back EMFs indicated as solid grey lines. This phenomenon can be utilized for rough estimation of the equivalent flat-top width. More accurate estimation will be presented and demonstrated in experimental results in the following. With the above derivation of current waveform under commutation phase error and nonideal back EMF, it is important to know that these two factors are independent with each other. The nonideal back EMF does not incur the shifting of the zero-crossing point.

C. CI Approach

This paper presents a reliable and useful method using the current waveform as an index for commutation phase error compensation. In the following derivation, delay commutation is considered, and lead commutation can be derived with the same token. The current waveform with time instant under delay commutation and nonideal back EMF waveform is shown in Fig. 5, where t_0 and t_2 are the beginning and the ending of the conducting period, respectively; T_α is the elapsed time of the nonflat area in one side of the back EMF. Note that the notation of time in lowercase letter represents time instant, while capital letter represents the elapsed time. The elapsed time of the commutation phase error, delay in this case, is defined as

$$T_{\text{error}} = |t_2 - t_{120}| \text{ or } T_{\text{error}} = |t_0 - t_{60}| \tag{17}$$

where t_{60} and t_{120} are the instants when the position of the rotor is at 60° and 120°, respectively. As shown in Fig. 5, t_{ba} is the beginning of the flat-top width of the back EMF of phase A; t_{bb} is the ending of the flat-top width of the back EMF of phase B. With the above definitions, the relationship between them can be shown as

$$t_{ba} = t_0 + (T_\alpha - T_{\text{error}}) \tag{18}$$

$$t_{bb} = t_2 - (T_\alpha + T_{\text{error}}). \tag{19}$$

With the same analogy in (3)–(5), during 60° –120° period, phases A and B are conducting, and phase C is floating. The

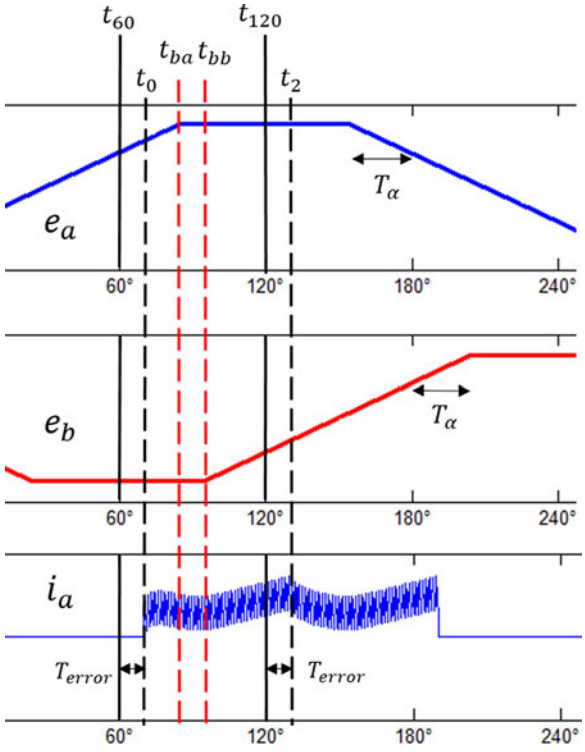

Fig. 5. Current waveform with time instant under delay commutation and nonideal back EMF.

current is shown as

$$i_a + \frac{L_s}{R_s}\frac{di_a}{dt} = \frac{V_{\text{bus}} \cdot S - (e_a - e_b)}{2R_s}. \tag{20}$$

From (12) and (13), the value of back EMFs can be shown as

$$e_a = \begin{cases} K_e\omega - \dfrac{6K_e\omega}{\pi + 6\alpha} \cdot \omega \cdot (t_{ba} - t) & \text{for } t_0 \le t < t_{ba} \\ K_e\omega & \text{for } t_{ba} \le t < t_2 \end{cases} \tag{21}$$

$$e_b = \begin{cases} -K_e\omega & \text{for } t_0 \le t < t_{bb} \\ -K_e\omega + \dfrac{6K_e\omega}{\pi + 6\alpha} \cdot \omega \cdot (t - t_{bb}) & \text{for } t_{bb} \le t < t_2 \end{cases}. \tag{22}$$

Substituting the back EMFs into (20) within different time region and integrating both sides of the equation from t_0 to t_2 gives

$$\begin{aligned} &\int_{t_0}^{t_2} R_s i_a(t) \cdot dt + L_s\left[i_a(t_2) - i_a(t_0)\right] = \frac{1}{2}\int_{t_0}^{t_2} V_{\text{bus}} \cdot S \cdot dt \\ &-\frac{1}{2}\left(\int_{t_0}^{t_{ba}} \left[K_e\omega - \frac{6K_e\omega}{\pi + 6\alpha} \cdot \omega \cdot (t_{ba} - t)\right] dt \right. \\ &\left. + \int_{t_{ba}}^{t_2} K_e\omega \cdot dt\right) + \frac{1}{2}\left(\int_{t_0}^{t_{bb}} (-K_e\omega) \cdot dt \right. \\ &\left. + \int_{t_{bb}}^{t_2} \left[-K_e\omega + \frac{6K_e\omega}{\pi + 6\alpha} \cdot \omega \cdot (t - t_{bb})\right] dt\right). \end{aligned} \tag{23}$$

Sorting out the V_{bus} part and the flat-top width part of the back EMF from the right-hand side of the equation gives

$$\begin{aligned}&\int_{t_0}^{t_2} R_s i_a(t)\cdot dt + L_s\left[i_a(t_2)-i_a(t_0)\right]\\&=\int_{t_0}^{t_2}\frac{V_{\text{bus}}\cdot S-2K_e\omega}{2}\cdot dt\\&+\frac{1}{2}\left(\int_{t_0}^{t_{ba}}\left[\frac{6K_e\omega}{\pi+6\alpha}\cdot\omega\cdot(t_{ba}-t)\right]dt\right.\\&\left.+\int_{t_{bb}}^{t_2}\left[\frac{6K_e\omega}{\pi+6\alpha}\cdot\omega\cdot(t-t_{bb})\right]dt\right).\end{aligned}\tag{24}$$

Integrating the nonflat width part of the back EMF and substituting the time definition into (18) and (19), we get

$$\begin{aligned}&\int_{t_0}^{t_2} R_s i_a(t)\cdot dt + L_s\left[i_a(t_2)-i_a(t_0)\right]\\&=\int_{t_0}^{t_2}\frac{V_{\text{bus}}\cdot S-2K_e\omega}{2}\cdot dt\\&+\frac{1}{2}\left(\frac{6K_e\omega}{\pi+6\alpha}\cdot\omega\cdot\frac{1}{2}\cdot\left[(T_\alpha-T_{\text{error}})^2+(T_\alpha+T_{\text{error}})^2\right]\right).\end{aligned}\tag{25}$$

Solving the two squares in the brackets of the right-hand side of the equation and separating the terms associated with T_α and T_{error} into two sides of the equation gives

$$\sqrt{\frac{A_1+A_2-B_1-B_2}{C_1}}=T_{\text{error}}\tag{26}$$

where

$$A_1=\int_{t_0}^{t_2} R_s i_a(t)\cdot dt,\quad A_2=L_s\left[i_a(t_2)-i_a(t_0)\right]\tag{26a}$$

$$B_1=\int_{t_0}^{t_2}\left(\frac{1}{2}V_{\text{bus}}\cdot S-K_e\omega\right)\cdot dt$$

$$B_2=\frac{1}{2}\left(\frac{6K_e\omega}{\pi+6\alpha}\cdot\omega\cdot T_\alpha^2\right)\tag{26b}$$

$$C_1=\frac{1}{2}\left(\frac{6K_e\omega}{\pi+6\alpha}\right)\omega.\tag{26c}$$

Assuming that T_α is known, we can extract the information of the commutation phase error from (26). Note that T_α is the function of the synchronous speed, and the average voltage applied to the motor can be expressed in terms of the duty ratio, defined as *D*, so (26b) can be further simplified as

$$B_1^*=\int_{t_0}^{t_2}\left(\frac{1}{2}V_{\text{bus}}\cdot D-K_e\omega\right)\cdot dt.\tag{27}$$

It is noted that the same result can be obtained for the lead commutation error. The components in the square root of the numerator in (26) contains four terms. The first two terms are about current waveform manipulation and defined as the CI. The third term is related to the supplied voltage and the motor speed, and the last term is related to the nonideal back EMF.

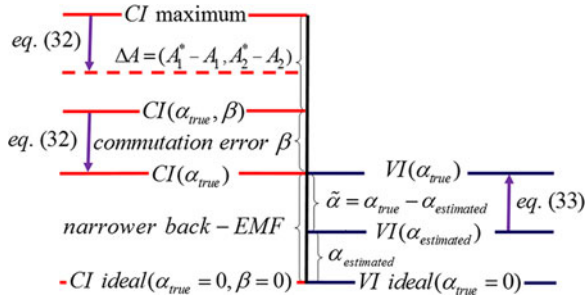

Fig. 6. Variations of CI and VI under the optimization process.

The summation of last two terms is defined as the voltage index (VI) for further discussion

$$\begin{aligned}&\text{Current Index (CI)}=A_1+A_2\\&=\int_{t_0}^{t_2} R_s i_a(t)\cdot dt + L_s\left[i_a(t_2)-i_a(t_0)\right]\end{aligned}\tag{28}$$

$$\begin{aligned}&\text{Voltage Index (VI)}=B_1+B_2\\&=\int_{t_0}^{t_2}\left(\frac{1}{2}V_{\text{bus}}\cdot S-K_e\omega\right)\cdot dt+\frac{1}{2}\left(\frac{6K_e\omega}{\pi+6\alpha}\cdot\omega\cdot T_\alpha^2\right).\end{aligned}\tag{29}$$

The causal effect of factors, α and β in (26) under constant speed can be expressed as

$$\sqrt{\frac{f_1(\alpha,\beta)+f_2(\alpha,\beta)-B_1^*-f_3(\alpha)}{f_4(\alpha)}}=T_{\text{error}}(\beta).\tag{30}$$

Unfortunately, this formula suffers from several drawbacks. First, the exact flat-top width of the approximated back EMF is the prerequisite for commutation phase error estimation. Second, the formula requires high sampling frequency to access precise current integration. Third, since the formula is also valid for lead commutation, T_{error} only reveals the magnitude without the knowledge of delay or lead commutation. Forth, the winding impedance is assumed to be a fixed value. These prerequisites limit the online implementation of the formula. Nevertheless, it is observed that (31) below always holds when $\alpha\le\alpha_{\text{true}}$due to the fact that $T_{\text{error}}\ge 0$

$$\sum\{A_1^*+A_2^*\}\ge\sum\{A_1+A_2\}\ge\sum\{B_1^*+B_2\}\tag{31}$$

$$A_1^*=\int_{t_0}^{t_2} R_{\max} i_a(t)\cdot dt\quad A_2^*=L_{\max}\left[i_a(t_2)-i_a(t_0)\right]\tag{31a}$$

where A_1^* and A_2^* are the values of A_1 and A_2, respectively, using estimated maximum values of resistance and inductance for particular applications. Thus, the parameter variations can be taken into consideration. The denominator in (26) is ignored because of the positive value. Examining (31), one observes that the magnitude of CI term contains three parts, as shown on the left-hand side of Fig. 6, i.e., the primary magnitude from the ideal current waveform, the increase from narrower back EMF and commutation phase error. The first term in VI will always

keep the same value under constant motor speed, while the second term will increase for narrow back EMF. Furthermore, from (28), the dominant term is the current integral A_1, which corresponds to the resistance effect; the boundary condition term A_2 corresponding to the inductance effect is relatively small and decreases with β, as can also be observed in Section III-A. The summation over several revolutions can minimize the influence from measurement noise, diminish the calculation error from speed fluctuation, and reduce the reliance on the sampling frequency of the microprocessor. Let us further define *J* as the difference between CI and VI. From (30), since T_{error} is only function of β, if the alpha used is set as $\alpha \leq \alpha_{\text{true}}$, the value of *J* will reach to minimum when the commutation phase error is fully compensated, or

$$\arg\min_{\beta} J(\alpha,\beta) = \min\{CI - VI\} \quad \text{for} \quad \alpha \leq \alpha_{\text{true}}. \quad (32)$$

Additionally, after the commutation phase error is compensated, *J* will decrease as the estimated alpha approaches to the true alpha, and the value will ideally reach to zero when the estimated alpha is correct, or

$$\arg\min_{\alpha} J(\alpha) = \min\{CI - VI\}. \quad (33)$$

In summary, the formula in (26) can extract the elapsed time of the commutation phase error. For increasing the feasibility of (26), the CI approach with (32) is developed for online implementation. Moreover, after the commutation phase error is fully compensated, *J* optimization in (33) can be further used for back EMF flat-top width estimation. The whole concept is depicted in Fig. 6, which describes the variations of CI and VI under the optimization process.

III. Simulation and Experimental Results

Simulation and experiment are conducted to show the effectiveness of the proposed CI approach. MATLAB and Simulink are used in simulation. The experiment prototype consists of a BLDC motor and power factor correction Kit (TMDSHVMTRPFCKIT) from Texas Instrument with DSP TMS320F28035. The motor is driven by a three-phase inverter consisting of six insulated gate bipolar transistors. The PWM switching frequency and the system sampling frequency under simulation and experiment are 20, 400, and 40 kHz, respectively; the sampling frequencies under simulation are set larger for precise integration results. The parameters used in this study are listed in Table I. As shown in Fig. 7, the control system consists of a line voltage differences method [3] to detect the zero-crossing points of back EMFs for the sensorless drive in the H_PWM_L_ON mode, a speed control loop using a proportional-integral controller with kp = 0.26 and ki = 2.5 in our case based on the Ziegler–Nichols closed-loop method [29], and a proposed commutation error correction loop, as indicated in a dashed box for J minimization. The synchronous speed is calculated from the time span of one electrical cycle and forced alignment is used as a starting procedure.

The organization of this section is as follows. First, the formula in (26) is testified in simulation to calculate the exact elapsed time of the commutation phase error. Second, the on-line commutation error compensation algorithm using the CI approach by (32) is demonstrated. Third, simulation studies are presented. Fourth, experiment results are demonstrated. Fifth, estimation of the equivalent flat-top width of the back EMF waveform is presented.

TABLE I
Motor Parameters

Rated Voltage	24 V
Rated Torque	0.127 N·m
Rated Power	53 W
Rated Speed	4000 rpm
Resistance	7 Ω
Inductance	0.66 mH
Rotor Inertia	4.80×10^{-6} kg·m^2
Back EMF Constant	2.07 V/krpm
Number of Poles	8

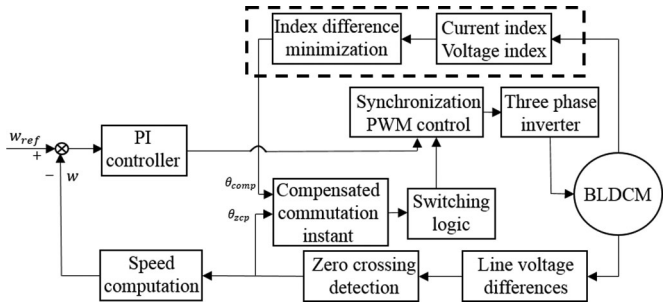

Fig. 7. Control system block diagram with the proposed commutation error correction method.

TABLE II
Investigation of the Elapsed Time of Commutation Phase Error by (26)

ω (rpm)	2050	2050	2050	500	500	500
$120 - 2\alpha$	120	120	70	120	120	80
Given β	0	21	21	0	5	5
$A_1 \times 10^4$	8.6	10.708	15.349	33.877	34	37.208
$A_2 \times 10^4$	0.0773	1.2228	1.6332	0.3151	0.3793	0.5421
$B_1{}^* \times 10^4$	8.6768	8.6768	8.6768	34.191	34.191	34.191
$B_2 \times 10^4$	0	0	4.7348	0	0	3.3333
C_1	1890.5	1890.5	2062.4	100	100	120
$T_{\text{error(msec)}}$	0.0051	0.4149	0.4161	0.0332	0.4339	0.4338
$\hat{\beta}_{(\text{deg})}$	0.2509	20.413	20.472	0.3984	5.2068	5.2
Error	N/A	−2.8%	−2.5%	N/A	4.0%	4.0%

A. Investigation of the Elapsed Time of the Commutation Phase Error by (26)

The current waveform is simulated first and the formula in (26) is applied to estimate the commutation phase error. Note that each term in (26) only calculates once with no average. Table II gives the result of each item inside the formula under different operational conditions, where the notations A_1, A_2, B_2, C_1, and B_1^* in the first column are defined in 26(a), (b), and (c) and (27). The simulation is tested under 500 and 2050 rpm; each of them is simulated under ideal and nonideal back EMF. Take the results under 2050 rpm for instance, the independent

variables α and β are separately set for the simulation. The first column presents the ideal case without any commutation phase error and under ideal back EMF, while the second column contains the factor of 21° delay commutation, and the third column contains two factors of 21° delay commutation and 70° flat back EMF. Comparing the first two columns, we observe that the CI increases with delay commutation β; the estimate $\hat{\beta}$ is calculated by $\omega \cdot T_{\text{error}}$. Comparing the second column and the third column, we observe that the increase in the CI is roughly the same as the rise in the α term, i.e., the fourth term of the numerator in (26); note that the slight difference between the CI and alpha term is due to the fact that the denominator is also a function of α. The estimated commutation phase error closely matches with the given value and only yields a small error ranging from -2.8% to 4.0%; the sources of error are the truncation error from numerical integration based on midpoint rule and the round off error in the current waveform simulation.

B. Commutation Phase Error Compensation Algorithm

Fig. 8 shows the flowchart of the online commutation phase error compensation approach. Given: x_0 as the initial step size of the algorithm, α_0 as the alpha used in the equation, C_0 as the tuning coefficient of the step size, *k* as the tuning stage of algorithm, *D* as the stopping threshold of the algorithm, *n* as the direction of the compensation, $J_{i,k,1}$ and $J_{i,k,2}$ as the first and the second *J* value at *i*th iteration and *k*th stage, respectively, and BoundFlag as the times when the algorithm reaches minimum. The step size is set as $x_k = (-1)^n\ C_0\ x_0$ for finer tuning; the resolution of the estimated commutation phase error is determined by the step size.

The algorithm first calculates the difference in (31) within appropriate revolution without compensating any commutation phase error and then calculates the value again after compensating x_k°. These two values are then compared with each other; if the second value decreases, the direction of compensation is correct and the algorithm will repeat the same procedure; otherwise, the direction of compensation should be reversed, i.e., $n = 1$. Once $J_{i,k,1}$ meets the minimum, in other words, $J_{i,k,2}$ is larger; the algorithm will count how many times it occurs, i.e., BoundFlag. At the same time, the algorithm will also compensate $-2x_k^\circ$ so that the algorithm can go back to the region where minimum occurs and prepare for finer tuning. As the BoundFlag reaches the setting value, the tuning stage *k* will increase by one and the step size will become smaller. At last, the algorithm ends when the tuning stage *k* is bigger than the stopping threshold *D*.

C. Simulation Results

In the proposed method, inductance variation is negligible due to its relatively small value as compared with the resistance term; however, such inductance variation can also be taken into account though. From (31), one knows that as long as the stator resistance used in the CI is larger than the real value, (31) will still hold true. Extensive simulation has been tested to investigate the effect of resistance variation on the performance of compensation. Two results under 2050 rpm with 21° delay angle and different real resistances are shown in Fig. 9. The real

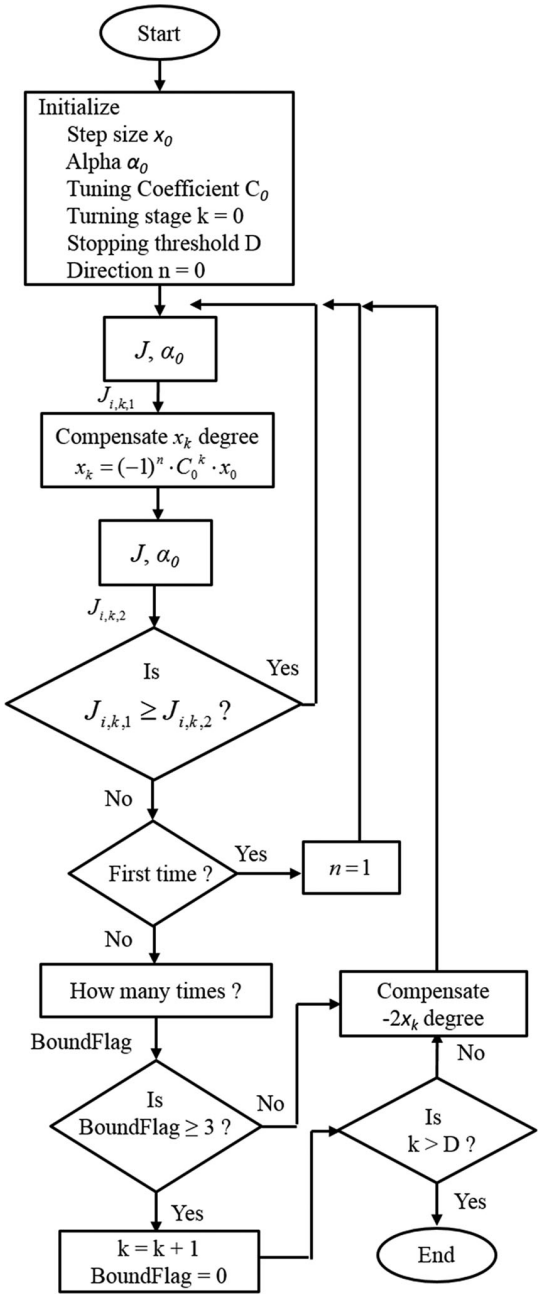

Fig. 8. Online commutation phase error compensation flowchart.

resistance values in the simulation are 8.4 and 9.8 Ω, while the maximum resistance value 10.5 Ω is used in the algorithm. The J-optimization will have different convergent value which depends on the maximum resistance value used and real pole width, however, it is always stable as long as the zero-crossing detection method is stable. The results demonstrate that J-optimization performs well by gradually pushing the delay angle from 21° to 0°.

D. Experiment Results

The online algorithm is tested under three speed zones: 500, 1250, and 2050 rpm. The initial step size, used alpha, tuning coefficient, stopping threshold, and BoundFlag, are set as 1,

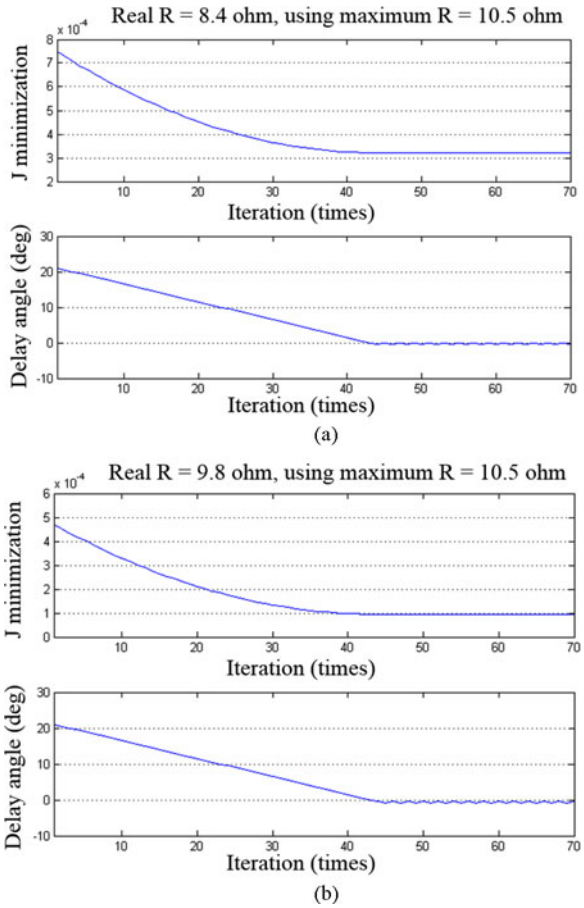

Fig. 9. J minimization under different resistance value at 2050 rpm. (a) Real R is 8.4 Ω and maximum R is 10.5 Ω. (b) Real R is 9.8 Ω and maximum R is 10.5 Ω.

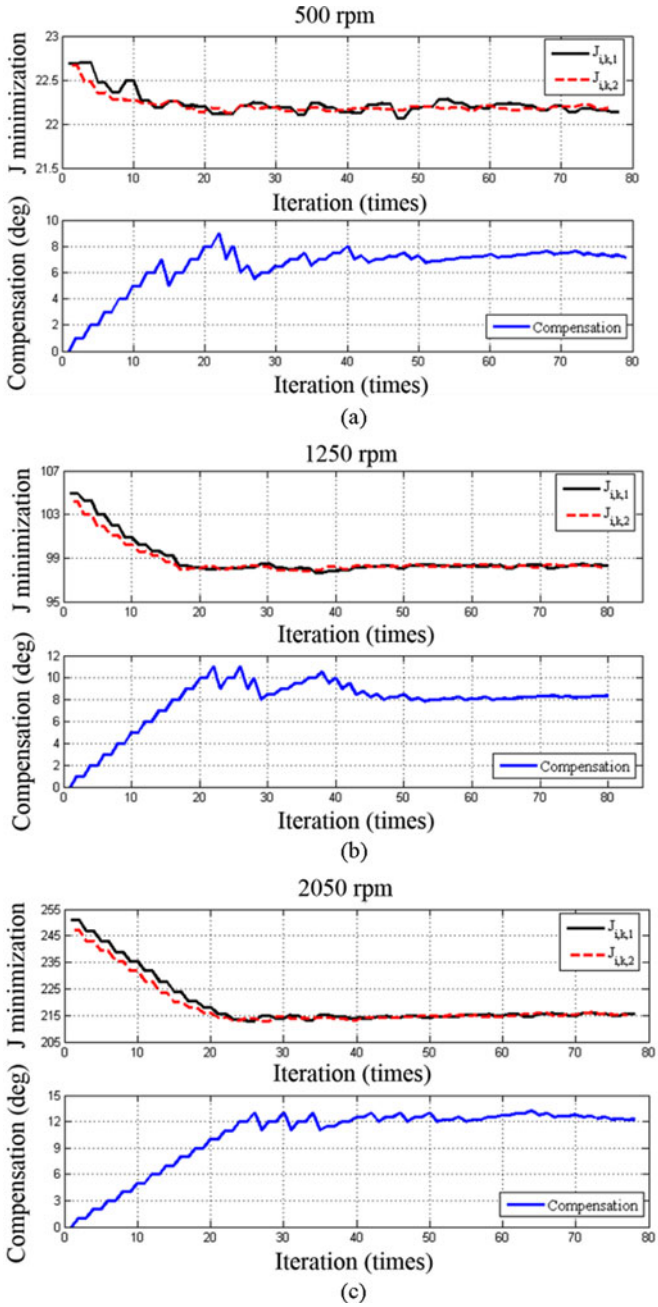

Fig. 10. Results of the online commutation phase error compensation algorithm under different speed. (a) J minimization versus compensation at 500 rpm. (b) J minimization versus compensation at 1250 rpm. (c) J minimization versus compensation at 2050 rpm.

0, 0.5, 3, and 3, respectively. In the experiment, the resistance value of 10.5 Ω is used in the online algorithm, while the tested motor stator resistance is 7 Ω. The currents are measured from current sensors with 40-kHz sampling frequency, two times of the PWM switching frequency. The CI and VI are calculated by summing 30 electrical revolutions, i.e., 7.5 rotor revolutions. Fig. 10 shows the J minimization, $J_{i,k,1}$ and $J_{i,k,2}$, and the compensation of the online algorithm under different speeds. The J minimization shows the decreasing trend with the decrease of the commutation phase error. The trend is more obvious at 1250 and 2050 rpm, since the amplitude of the back EMF is proportional to the synchronous speed and the sensorless drive is more stable in the high-speed operation. Furthermore, one can observe that the higher the speed, the larger the delay angle needed to be compensated, i.e., from 8° to 12°. The current waveforms before and after J minimization at different speeds are shown in Fig. 11.

As discussed in Section III, before any compensation, the pulsating current results in larger CI. After compensating the commutation phase error, the current waveform coincides with the ideal waveform and the J value reaches to minimum. In Fig. 11(c), the peak values of the current at the front and back of the current waveform at each conducting period are defined as $\boldsymbol{If}$ and $\boldsymbol{Ib}$. The current ratio indicating the accurateness of commutation instant is defined as follows:

$$\text{Currentratio} = \frac{\boldsymbol{If}}{\boldsymbol{Ib}} \tag{34}$$

that becomes one when minimum torque ripple occurs. Figs. 12 and 13 show the performance of the proposed method at different speeds and load torque. Dotted and solid lines represent before

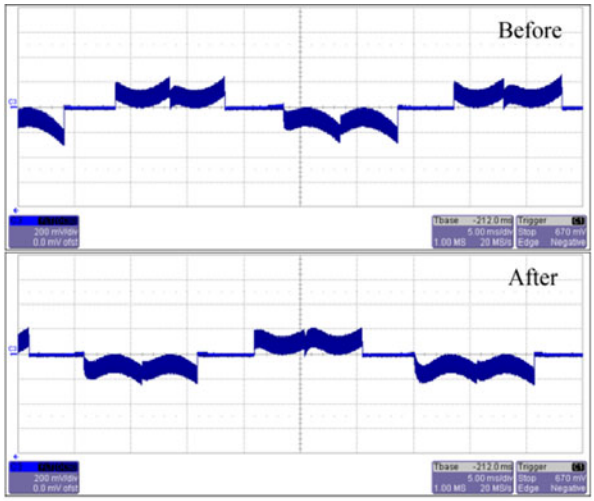

(a)

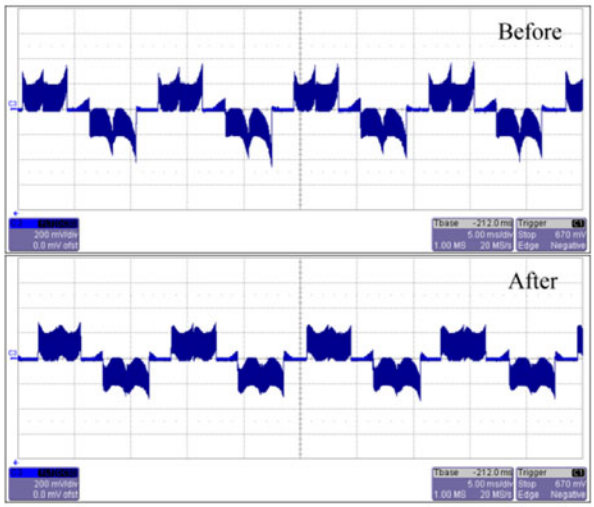

(b)

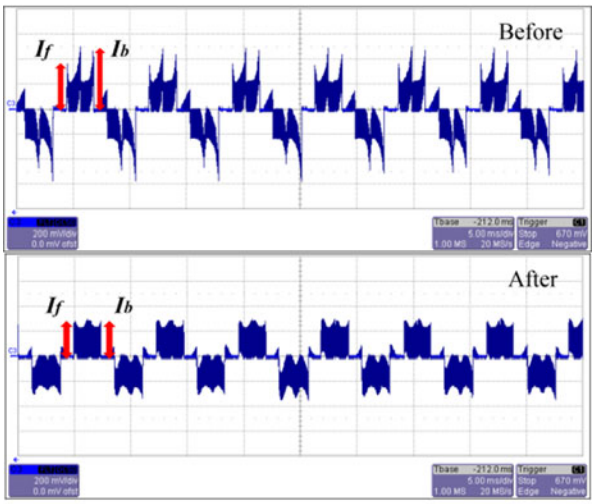

(c)

Fig. 11. Current waveform of phase A before and after compensation under different speed. (a) 500 rpm (*x*-axis: 5 ms/div, *y*-axis: 200 mA/div). (b) 1250 rpm (*x*-axis: 5 ms/div, *y*-axis: 200 mA/div). (c) 2050 rpm (*x*-axis: 5 ms/div, *y*-axis: 200 mA/div).

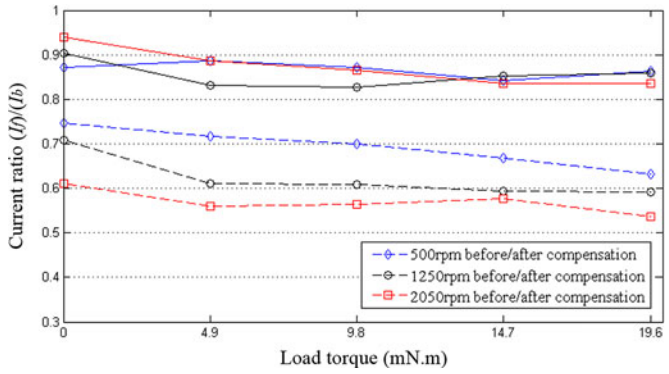

Fig. 12. Performance of the CI commutation error compensation under different speed and load torque. Dotted and solid lines represent before and after compensation.

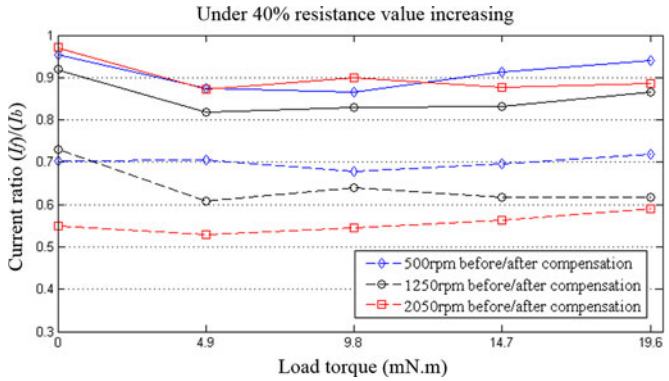

Fig. 13. Performance of CI commutation error compensation due to 40% increase in the resistance at different speed and load torque. Dotted and solid lines represent before and after compensation.

and after compensation, respectively. For the case of Fig. 12, the normal motor with resistance 7 Ω is tested. For the case of Fig. 13, for simulating the increase of the resistance value with the operating temperature, 40% increase in the resistance is in series externally with each motor phase, and hence, the motor resistance becomes 9.8 Ω. Note that the resistance value used in the algorithm for both cases is 10.5 Ω. Experiment results showed that the method is capable of running in different speeds and load torque with good performance and is robust to parameter variation, as long as the resistance value used in the algorithm is larger than the real value.

E. Equivalent Flat-Top Width of the Back EMF Experiment

While the CI value has reached to its minimum, the VI value will reach the same value as CI when the estimated alpha is equal to the actual alpha in the motor. Hence, an algorithm for equivalent flat width derivation is presented, as shown in Fig. 14. The concept of the algorithm is similar to the one for commutation phase error compensation; the estimated alpha keeps iterating till the stopping threshold is satisfied. The exact or equivalent alpha is then calculated as $\alpha_0 + (i - p - 1)\, d^\circ$.

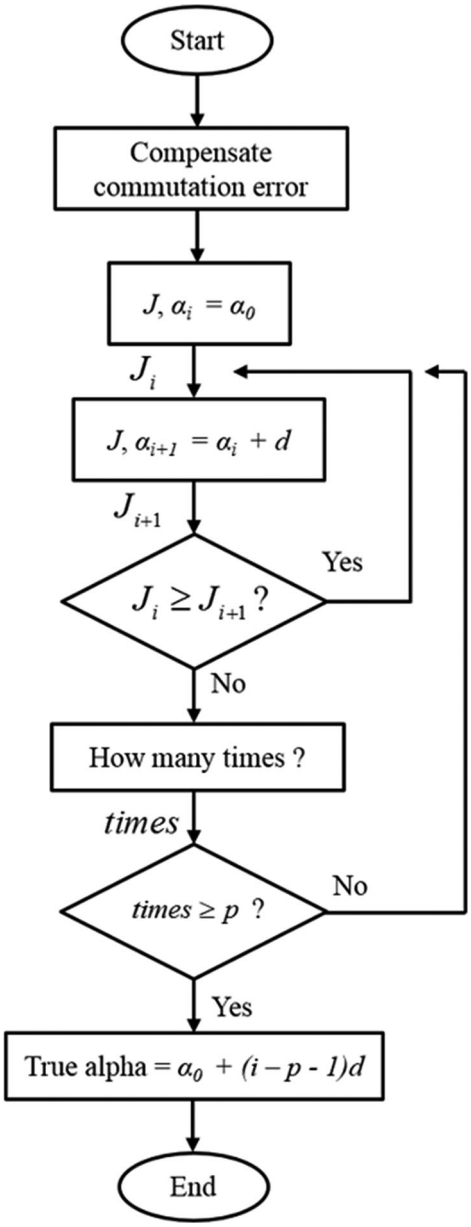

Fig. 14. Equivalent back EMF flat-top width estimation flowchart.

Since the equivalent flat-top width of the back EMF only need to be identified once, the current waveform is captured from the oscilloscope with 2-MHz sampling frequency and the algorithm is executed in MATLAB. The initial alpha, step size, and the stopping threshold are given as 0, 0.5, and 10, respectively. The algorithm is tested under 500, 1250, and 2050 rpm; the average results of the estimated alpha is 25°. The estimated equivalent flat-top width of the back EMF is thus 70°. Fig. 15 gives the comparing results between the simulated current waveform under 70° flat back EMF and the real current waveform captured from the oscilloscope at 1250 rpm. The result shows great resemblance. The commutation torque ripple, indicated in the dashed box, is due to asynchronous PWM switching, which requires further control technique [30].

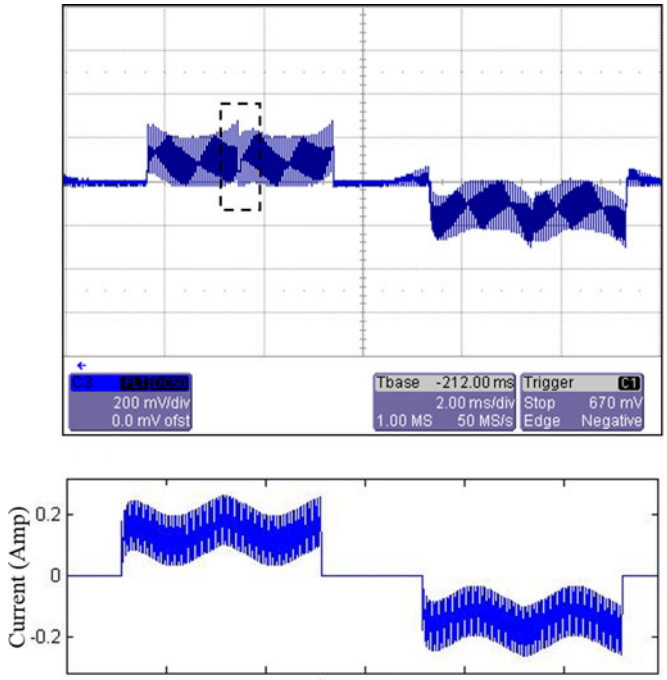

Fig. 15. Real current waveform versus simulated current waveform under 70° flat back EMF at 1250 rpm. (*x*-axis: 2 ms/div, *y*-axis: 200 mA/div).

IV. Conclusion

The current waveform under commutation phase error and nonideal back EMF are being analyzed in depth in this study. An optimization approach using the current waveform as an index is proposed to compensate the commutation phase error. The influence of parameter variation to this method is also discussed; simulation and experimental results are shown to testify the robustness of this method under parameter variation due to operating condition. Experimental results show the effectiveness of the proposed method under different speed, load torque, and parameter variation. In addition, the proposed method can be utilized for equivalent flat-top width estimation.

References

[1] J. C. Gamazo-Real, E. Vázquez-Sánchez, and J. Gómez-Gil, "Position and speed control of brushless dc motors using sensorless techniques and application trends," *Sensors*, vol. 10, pp. 6901–6947, 2010.

[2] K. Iizuka, H. Uzuhashi, M. Kano, T. Endo, and K. Mohri, "Microcomputer control for sensorless brushless motor," *IEEE Trans. Ind. Appl.*, vol. IA-21, no. 3, pp. 595–601, May 1985.

[3] P. Damodharan and K. Vasudevan, "Sensorless brushless dc motor drive based on the zero-crossing detection of back electromotive force (EMF) from the line voltage difference," *IEEE Trans. Energy Convers.*, vol. 25, no. 3, pp. 661–668, Mar. 2010.

[4] T. Kim, C. Kim, and J. Lyou, "A new sensorless drive scheme for a BLDC motor based on the terminal voltage difference," in *Proc. IEEE. Ind. Electron. Soc. Conf.*, 2011, pp. 1710–1715.

[5] J. Shao, D. Nolan, and T. Hopkins, "A novel direct back EMF detection for sensorless brushless dc (BLDC) motor drives," in *Proc. IEEE Appl. Power Electron. Conf. Expo.*, 2002, pp. 33–38.

[6] J. C. Moreira, "Indirect sensing for rotor flux position of permanent magnet ac motors operating over a wide speed range," *IEEE Trans. Ind. Appl.*, vol. 32, no. 6, pp. 1394–1401, Nov.–Dec. 1996.

[7] S. Ogasawara and H. Akagi, "An approach to position sensorless drive for brushless DC motors," *IEEE Trans. Ind. Appl.*, vol. 27, no. 5, pp. 928–933, Sep.–Oct. 1991.
[8] Z. M. A. Peixo, F. M. F. Sa, P. F. Seixas, B. R. Menezes, P. C. Cortizo, and W. S. Lacerda, "Application of sliding mode observer for induced e.m.f., position and speed estimation of permanent magnet motors," in *Proc. Int. Conf. Power Electron. Drive Syst.*, 1995, vol. 2, pp. 599–604.
[9] T. S. Kim, B. G. Park, D. M. Lee, J. S. Ryu, and D. S. Hyun, "A new approach to sensorless control method for brushless DC motors," *Int. J. Control Autom. Syst.*, vol. 6, pp. 477–487, 2008.
[10] R. Dhaouadi, N. Mohan, and L. Norum, "Design and implementation of an extended Kalman filter for the state estimation of a permanent magnet synchronous motor," *IEEE Trans. Power Electron.*, vol. 6, no. 3, pp. 491–497, Jul. 1991.
[11] T. H. Kim and M. Ehsani, "An error analysis of the sensorless position estimation for BLDC motors," in *Proc. Conf. Rec. Ind. Appl. Conf.*, 2003, vol. 1, pp. 611–617.
[12] A. H. Niasar, A. Vahedi, and H. Moghbelli, "A novel position sensorless control of a four-switch, brushless dc motor drive without phase shifter," *IEEE Trans. Power Electron.*, vol. 23, no. 6, pp. 3079–3087, Nov. 2008.
[13] J. X. Shen and K. J. Tseng, "Analyses and compensation of rotor position detection error in sensorless PM brushless DC motor drives," *IEEE Trans. Energy Conver.*, vol. 18, no. 1, pp. 87–93, Mar. 2003.
[14] K. Y. Cheng and Y. Y. Tzou, "Design of a sensorless commutation IC for BLDC motors," *IEEE Trans. Power Electron.*, vol. 18, no. 6, pp. 1365–1375, Nov. 2003.
[15] D. H. Jung and I. J. Ha, "Low-cost sensorless control of brushless DC motors using a frequency-independent phase shifter," *IEEE Trans. Power Electron.*, vol. 15, no. 4, pp. 744–752, Jul. 2000.
[16] G. J. Su and J. W. Mckeever, "Low-cost sensorless control of brushless dc motors with improved speed range," *IEEE Trans. Power Electron.*, vol. 19, no. 2, pp. 296–302, Mar. 2004.
[17] T. W. Chun, Q. V. Tran, H. H. Lee, and H. G. Kim, "Sensorless control of BLDC motor drive for an automotive fuel pump using a hysteresis comparator," *IEEE Trans. Power Electron.*, vol. 29, no. 3, pp. 1382–1391, May 2013.
[18] Q. Jiang, C. Bi, and R. Huang, "A new phase-delay-free method to detect back EMF zero-crossing points for sensorless control of spindle motors," *IEEE Trans. Magn.*, vol. 41, no. 7, pp. 2287–2294, Jul. 2005.
[19] S. Bhogineni and K. R. Rajagopal, "Position error in sensorless control of brushless dc motor based on average line to line voltages," in *Proc. IEEE Int. Conf. Power Electron., Drives Energy Syst.*, 2012, pp. 1–6.
[20] N. Urasaki, T. Senjyu, K. Uezato, and T. Funabashi, "Adaptive dead-time compensation strategy for permanent magnet synchronous motor drive," *IEEE Trans. Energy Convers.*, vol. 22, no. 2, pp. 271–280, Jun. 2007.
[21] G. H. Jang, J. H. Park, and J. H. Chang, "Position detection and startup algorithm of a rotor in a sensorless BLDC motor utilising inductance variation," *Proc. Inst. Elect. Eng.—Electr. Power Appl.*, vol. 149, no. 2, pp. 137–142, Mar. 2002.
[22] G. H. Jang and M. G. Kim, "Optimal commutation of a BLDC motor by utilizing the symmetric terminal voltage," *IEEE Trans. Magn.*, vol. 42, no. 10, pp. 3473–3475, Oct. 2006.
[23] X. Wu, B. Zhou, F. Song, F. Chen, and J. Wei, "A closed loop control method to correct position phase for sensorless Brushless DC motor," in *Proc. Int. Conf. Electr. Machines Syst.*, 2008, pp. 1460–1464.
[24] G. Meng, H. Xiong, and H. Li, "Commutation torque ripple reduction in BLDC motor using PWM_ON_PWM mode," in *Proc. Int. Conf. Electr. Mach. Syst. Conf.*, 2009, pp. 1–6.
[25] J. Fang, W. Li, and H. Li, "Self-compensation of the commutation angle based on dc-link current for high-speed brushless DC motors with low inductance," *IEEE Trans. Power Electron.*, vol. 29, no. 1, pp. 428–439, Jan. 2014.
[26] J. H. Song and I. Choy, "A rotor position sensorless control based on neutral voltage compensation," in *Proc. IEEE 35th Power Electron. Spec. Conf.*, Jun. 2004, vol. 2, pp. 1431–1437.
[27] H. C. Chen and C. M. Liaw, "Sensorless control via intelligent commutation tuning for brushless dc motor," *Inst. Electron. Eng. Electron. Power Appl.*, vol. 146, no. 6, pp. 678–684, 2002.
[28] T. M. Jahns and W. L. Soong, "Pulsating torque minimization techniques for permanent magnet ac motor drives—A review," *IEEE Trans. Power Electron.*, vol. 43, no. 2, pp. 321–330, Apr. 1996.
[29] N. F. Macia, and G. J. Thaler, *Modeling and Control of Dynamic Systems*. New York, NY, USA: Thomson Delmar Learning, 2005.
[30] D. K. Kim, K. W. Lee, and B. I. Kwon, "Commutation torque ripple reduction in a position sensorless brushless dc motor drive," *IEEE Trans. Power Electron.*, vol. 21, no. 6, pp. 1762–1768, Nov. 2006.

An-Chen Lee received the B.S. and M.S. degrees in power mechanical engineering from National Tsing Hua University, Hsinchu, Taiwan, in 1978 and 1980, respectively, and the Ph.D. degree in mechanical engineering from the University of Wisconsin-Madison, Madison, WI, USA, in 1986.

He is designated as the Chair Professor of National Chiao Tung University, Hsinchu, and is currently a Professor in the Department of Mechanical Engineering. His current research interests include computer numerical control machine tool control technology, magnetic bearing technology, rotor dynamic and control, and semiconductor manufacturing process control. He served as an Editorial Board Member of the *International Journal of Precision Engineering and Manufacturing* and the *Journal of Chinese Society of Mechanical Engineers*.

Dr. Lee received the National Science Committee (NSC) Excellent Research Award (1991–1992), NSC Distinguished Research Award (1993–1994, 1995–1996, 1997–1998), NSC Research Fellow (1999–2001, 2002–2004), NSC research fellow Award (2005), Chinese Society of Mechanical Engineers Distinguished Engineering Professor Award (2001), Gold Medal Award, Inventor/New Product Exposition (INPEX), Pittsburgh, PA, USA (2010), Gold Medal Award, and International Exhibition of Inventions of Geneva (2011).

Samuel Wang was born in California, USA, in 1990. He received the B.S. degree in mechanical engineering from National Chiao Tung University, Hsinchu, Taiwan, in 2012, where he is currently working toward the M.S. degree in mechanical engineering.

Chia-Juei Fan was born in Taipei, Taiwan, in 1991. He received the B.S. degree in mechanical engineering from National Chung Cheng University, Chiayi, Taiwan, in 2013. He is currently working toward the M.S. degree in mechanical engineering from National Chiao Tung University, Hsinchu, Taiwan.